J. Fluid Mech. (1983), *vol.* 126, *pp.* 187–204
Printed in Great Britain

Instantaneous pressure fields at a corner associated with vortex impingement

By Y.-P. TANG† AND D. ROCKWELL

Department of Mechanical Engineering and Mechanics, Lehigh University,
Bethlehem, PA

(Received 20 November 1981)

The impingement of concentrations of vorticity upon a corner is studied using simultaneous flow visualization and correlation of pressure fluctuations, revealing the relations between the instantaneous pressure fields along the top and front faces of the corner and the instantaneous distortion of the incident vortex.

By varying the transverse offset of the corner relative to the incident vortex, several distinct and consistent patterns of incident vortex–corner interaction are evident. The corresponding form and phasing of the instantaneous pressure fields are strongly dependent upon the nature of the vortex–corner interaction, though the maximum amplitude on the top and front faces is always of the same order. For certain interactions, there is separation of flow from the edge of the corner, as well as from the front face of the corner, leading to secondary-vortex formation and corresponding peaks in the local pressure fields.

By integrating the instantaneous pressure fields along the top and front faces of the corner, the phasing between the respective forces is shown to exhibit varying degrees of dipole-like behaviour, depending upon the character of the incident vortex–corner interaction. Amplitudes of the corresponding moments of the pressure fields are remarkably insensitive to this interaction.

1. Introduction

The nature of large-scale coherent structures in unstable laminar and turbulent shear layers has received considerable attention (see the review of Roshko 1976), but the interaction between these vortical structures and various surfaces is not well understood (Rockwell 1982). Such interactions are central to characterizing the dynamic loading of the surface and the associated noise generation. Recent studies in this direction include vortex– (slender) leading-edge interaction (Ziada & Rockwell 1982), as well as the nature of the unsteady shear layer upstream of a corner configuration (Rockwell & Knisely 1979; Knisely & Rockwell, 1982). These investigations show that insertion of an edge or corner in the shear layer has a deterministic role in organizing the flow events in upstream regions of the shear layer. However, the relationship between distortion of vortices incident upon an edge or corner and the induced pressure fields along the corresponding surfaces has remained uninvestigated.

The purpose of this investigation is to visualize the distortion of vortices incident upon a corner for various transverse locations of the corner with respect to the incident vortex, as well as associated concentrations of (opposite) vorticity arising

---

† Present address: Air Products and Chemicals, Inc., Trexlertown, PA.

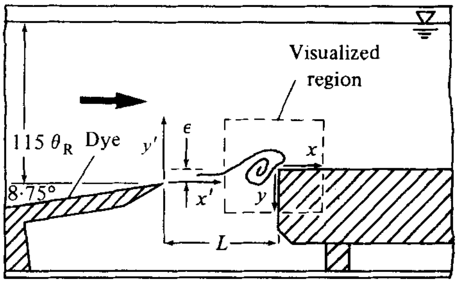

Side view

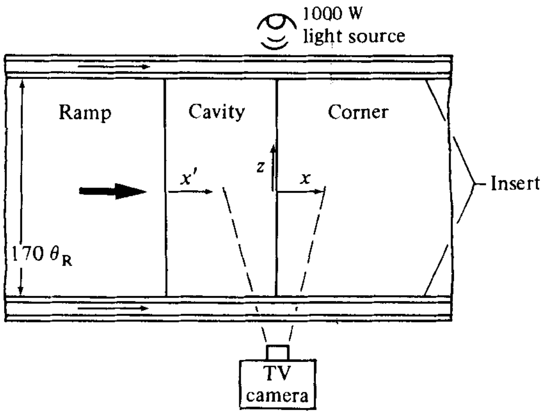

Top view

FIGURE 1. Overall view of the experimental test section and lighting arrangement for visualization.

from the corner interaction; simultaneously, the instantaneous pressure fields are characterized, allowing detailed insight into the intimate relation between vortex interaction and induced pressure.

2. Experimental systems and techniques

2.1. *Test section and flow parameters*

To ensure that the vortex–corner interactions were repeatable, thereby providing periodic pressure fields at the impingement corner, the following conditions had to be satisfied in the design of the test section: a constant frequency of vortex shedding from the upstream edge of the cavity; an essentially two-dimensional vortex structure approaching and interacting with the corner; and a consistent interaction pattern of the successively incident vortices. As pointed out by Knisely & Rockwell (1982), attainment of this last condition is difficult at longer impingement lengths L or higher flow speeds U (see figure 1), in that there is 'jitter' or irregularity in the vortex-impingement pattern. This effect was essentially precluded by selecting a relatively short cavity length ($L = 31\theta_R$) and a free-stream velocity of $U = 18{\cdot}3$ cm/s.

A reference momentum thickness $\theta_R = 0{\cdot}14$ cm was defined at the streamwise station $18\theta_R$ upstream of the impingement corner. This compares with the value of momentum thickness of the boundary layer separating from the upstream edge of the cavity, $\theta_0 = 0{\cdot}078$ cm. The height and streamwise length of the downstream impingement corner (figure 1) were $36\theta_R$ and $340\theta_R$ respectively. Owing to the relatively long length of this 'outlet' of the cavity, there was virtually no mean flow between the corner insert and the bottom wall of the test section.

Reynolds numbers of the flow approaching the corner were $Re_{\theta_0} = 141$ and $Re_{\theta_R} = 257$. Power spectra of free-stream velocity fluctuations revealed a total (integrated spectral) turbulence level of less than 0·1 %, concentrated primarily at frequencies well below those of interest in the study. Moreover, it should be noted that extensive velocity spectra were acquired in the free stream to insure there was no contamination from free-surface effects (Knisely & Rockwell 1982).

In order to examine a range of vortex–corner interaction patterns, it was necessary to select several different vertical offsets of the impingement corner relative to the upstream separation edge of the cavity. High, medium and low corner positions corresponded to $\epsilon/\theta_R = 3{\cdot}3$, $1{\cdot}1$ and $-1{\cdot}1$ respectively, where ϵ is defined in figure 1. For all three corner offsets the vortex-shedding frequency remained the same, having a value of $f\theta_R/U = 0{\cdot}0217$ and $f\theta_0/U = 0{\cdot}0120$. The phase speeds of the vortices approaching the corner were determined from streamwise phase measurements at the upper edge of the mean shear layer. The average phase speed determined from hot-film phase measurements was $c/U = 0{\cdot}48 \pm 10\,\%$; the corresponding value of wavelength of the incident vortices determined independently from visualization was $\lambda/\theta_R = 20 \pm 10\,\%$.

2.2. *Visualization technique*

Vortex impingement upon the corner was visualized using the dye-injection technique. Food-colour dye was laid on the surface of the acceleration ramp to generate continuous streaklines. An Instar dual-camera television system having vertical and horizontal sweep frequencies of 120 and 25·2 Hz respectively, with split-screen capability, recorded the corner region activity and the simultaneous pressure/velocity fluctuation traces were displayed on a storage oscilloscope. At a framing rate of 120 frames/s and a resolution of 250 lines, the recording had an uncertainty due to the finite time between frames of $\pm 1{\cdot}2\,\%$ of the period of vortex formation. All photos shown herein were obtained by taking 4 in. × 5 in. Polaroids of the image on the video screen at approximately the same scale unless otherwise stated.

2.3. *Device for measurement of surface-pressure fluctuations*

In the immediate region of the corner, large streamwise gradients of pressure can occur, depending on the nature of vortex distortion. Consequently, a design incorporating a rotating-disk arrangement was constructed to measure pressure at a relatively large number of stations over a small area near the corner. The model consists of two pressure 'valves', one on the top, the other on the front face of the corner; only the top face arrangement is described here. The components are an outer brass cover plate, a brass disk, and a thin rubber gasket as shown in figure 2. The main element is the thin flanged disk with thirteen 0·16 cm diameter holes drilled through its surface to serve as pressure taps; they are arranged in a pattern designed to achieve the desired 'effective' spacing of pressure taps. That is, the angular spacing between adjacent holes is determined so that a sector covered by each hole does not overlap with that covered by the adjacent ones. Each of these thirteen holes is located

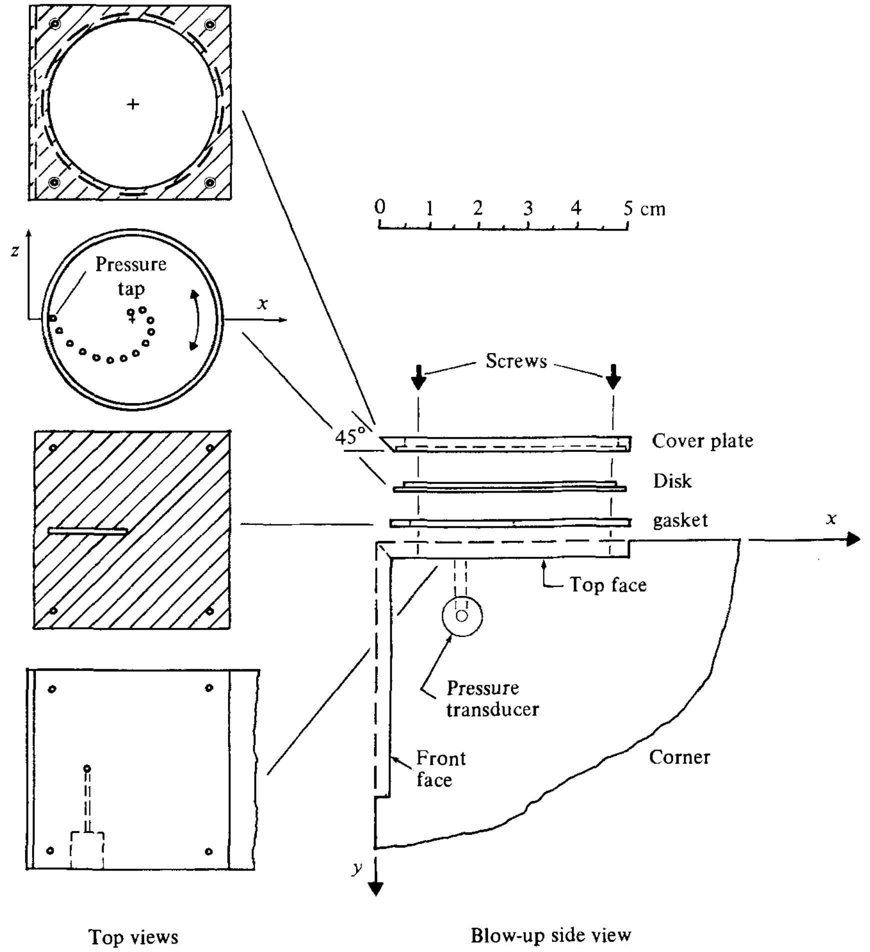

FIGURE 2. Rotating-disk arrangement for measurement of distributions of fluctuating pressure over small domains near the edge of the corner.

at a different radial distance from the disk centre, with an increment of 0·16 cm to form a spiral pattern, covering a complete revolution. Placed underneath the disk is a thin rubber gasket with a 0·16 cm × 2·06 cm slot. A 5·72 cm square cover plate with a circular cutout is used to hold the disk and the gasket together against the Plexiglas corner structure by means of four screws. A 0·16 cm diameter circular passage is drilled at the middle of the channel cut into the Plexiglas corner to connect with the side-mounted pressure transducer. Thus a pressure tap can be positioned at any of thirteen discrete locations along a streamwise line by simply rotating the disk. Although not shown in figure 2, the vertical surface of the corner is equipped with an assembly identical with that described above, in order to provide simultaneous pressure measurement on both surfaces of the corner.

Each pressure-valve system was tested in a water channel with zero flow to determine its natural frequency and damping ratio. A Kulite XCS-190-2D pressure transducer having its diaphragm coated with Paralene was selected because of its small size and high natural frequency of 100 kHz. Transient responses for both the top valve system (shown in figure 2), as well as the front valve system (i.e. on the front face of the corner), subjected to an impulse input, were recorded simultaneously, and the corresponding cross-spectrum computed digitally. Results showed that the natural frequency is about 22 Hz, with a damping ratio of no more than 0·07 for all taps. This corresponds to amplitude and phase distortions of 2 % and 1·2° respectively at the shedding (fundamental) frequency of interest in the present investigation. The length of line from a given tap to the face of the pressure transducer varies, depending on the tap chosen, but negligible time delay was measured between the front and the top tap when the maximum difference in passage length was chosen.

To allow measurements very close to the corner, two other corner pieces were built with fixed pressure taps positioned on both the front and top faces at $0{\cdot}06\lambda$ (0·16 cm) and $0{\cdot}12\lambda$ (0·32 cm) from the edge of the corner, where λ is the wavelength of the incident vortices. Amplitude and phase distortion were also found to be negligible due to the small length-to-diameter ratio of the lines. Further details are described by Tang (1981).

2.4. *Measurement techniques*

A three-part measuring procedure allowed determination of both amplitude and relative phase of each local pressure fluctuation. First, for pressure measurement on the front face of the corner, the leading tap on the top face was used to provide a reference signal, recorded simultaneously with each of the seven pressure signals from the front face. Secondly, the reverse was carried out; the leading tap on the front face served as reference tap in order to obtain pressure measurement on the top face. Finally, pressure measurements were taken 'diagonally', using taps on both surfaces having the same distance from the edge of the corner. Therefore a total of 21 sets of effectively simultaneous pressure signals were acquired. As for measurement very close to the edge, using the two corner pieces having fixed pressure taps located distances of 0·16 cm and 0·32 cm from the edge, a hot-film probe positioned at a fixed location near shear-layer separation ($x' = 0$ in figure 1) provided a reference signal: such a phase reference is necessary in relating these measurements to those acquired with the rotating-disk system.

All the pressure signals and their accompanying reference signals were digitized, recorded, then processed using a cross-spectrum program to determine their amplitude and relative phase. Each sample contained approximately 115 cycles of oscillation, and the resultant ensemble-averaged spectrum had a frequency resolution of 0·16 Hz. The deliberate redundancy of the above measurement procedure allowed cross-checking of the amplitude and phase measurements.

Velocity measurements were taken by means of DISA hot-film probes (55R14) using a DISA 55D01 anemometer in conjunction with a DISA 55M25 linearizer. Velocity and pressure signals were filtered with negligible phase shift at the fundamental frequency of vortex formation and amplified by Krohn–Hite Model 3700 bandpass filters and class A variable-gain amplifiers.

A MINC computer with a usable RAM memory of 28 K allowed real-time spectral analysis. Resultant velocity or pressure spectra were ensemble-averaged (over 5 independent spectra) for improved statistical validity and displayed on a CRT terminal. On the other hand, most pressure signals, along with a simultaneous reference signal (either velocity or pressure signal), were sampled, digitized and stored on cassettes using a digital oscilloscope (Nicolet 1090A, 4 K memory) in conjunction with an interface (Nicolet 232C) and a data cassette recorder (Techtran 8410). The stored data were later transferred to magnetic tapes and processed on a CDC 6400 digital computer via a cross-spectrum technique to determine the amplitude and phase of the pressure signal with respect to the reference signal.

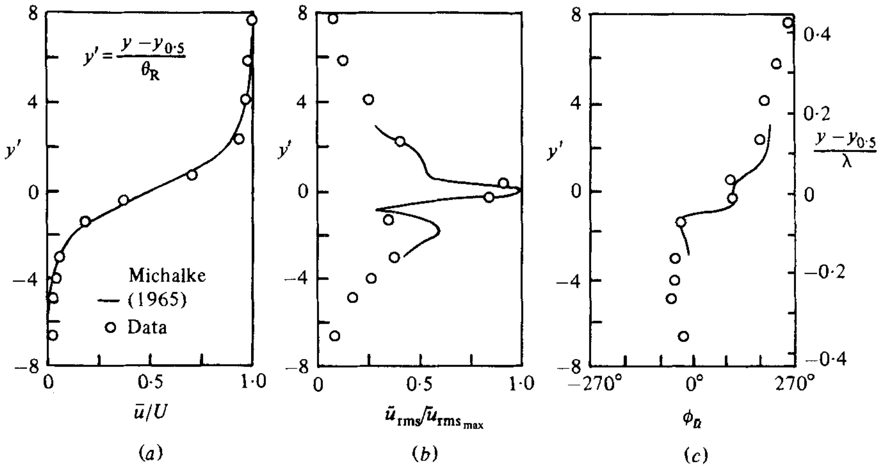

FIGURE 3. Profiles of mean and fluctuation parameters of the approach shear layer: (*a*) normalized mean-velocity profile; (*b*) normalized distribution of longitudinal velocity fluctuation; (*c*) phase distribution of the longitudinal velocity fluctuation. All distributions taken at reference station $x'/\theta_R = 13$. $\epsilon/\theta_R = 1{\cdot}1$, $L/\theta_R = 31$.

3. Nature of unsteady shear layer incident upon corner

To characterize the unsteadiness incident upon the impingement corner, a reference station was chosen at a distance of approximately one disturbance wavelength upstream of impingement corresponding to $18\theta_R$, where $\theta_R = 1{\cdot}8\theta_0$; moreover, at this location, the amplifying disturbance had reached its saturation value. Distortion of the fluctuating vorticity field due to the downstream corner is negligible at this reference station; in a related study, Rockwell & Knisely (1979) found, using laser anemometry and hydrogen-bubble techniques, that the convective velocity and distortion of the incident vortex were influenced only very near the corner – less than one wavelength upstream of it. Normalizing parameters employed herein are the reference momentum thickness θ_R and the wavelength λ of the shear layer approaching the corner. Figure 3(*a*) shows the mean-velocity profile at the reference station, compared with the hyperbolic tangent profile $\frac{1}{2}(\bar{u}/U)\,[1+\tanh\,(y-y_{0.5})/2\theta]$ (Michalke 1965). In figures 3(*b, c*) the distributions of longitudinal velocity fluctuation $\tilde{u}_{rms}$ and its phase $\phi_{\tilde{u}}$ are compared with respective theoretical profiles calculated using the linear inviscid theory of Michalke (1965) at the local Strouhal number $f\theta_R/U = 0{\cdot}022$. The maximum value of $\tilde{u}_{rms}(y)$ is designated as $\tilde{u}_{max}$ $(= 0{\cdot}06U)$, employed in defining the amplitude of pressure fluctuation $\tilde{p}_{rms}$. With these well-posed conditions of the approach shear layer, the unsteady pressure field at the corner can be scaled accordingly.

4. Instantaneous pressure fields

Representations of the instantaneous fluctuating pressure in the vicinity of the corner, shown in figures 4(*a–c*), were constructed using corresponding time-averaged amplitude and phase information (Tang 1981). The variations of these instantaneous pressure distributions with time, over one cycle of oscillation, are represented in $\frac{1}{8}$-cycle intervals, starting at the top of figures 4(*a–c*). As shown, each pressure schematic is a composite of pressure distributions on both faces of the corner, with the front-face (y-axis) pressure distribution angled to the left, and the top-face (x-axis) distribution displayed horizontally to the right; together these distributions form an isometric

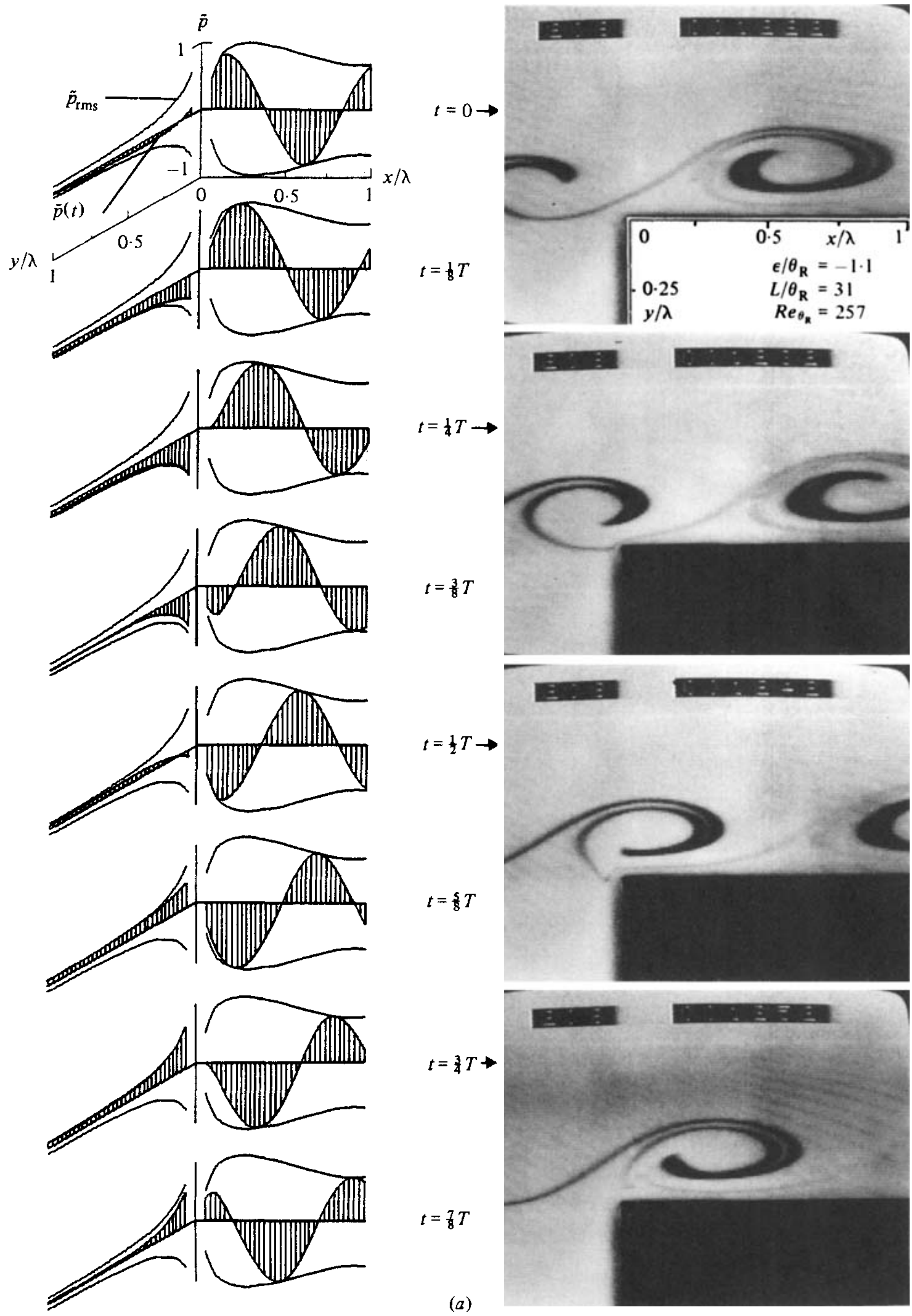

(*a*)

FIGURE 4. For caption see p. 195.

view of the corner. (Note the blank region extremely close to the corner of extent $\sim 0{\cdot}06\lambda$, where no pressure taps could be instrumented.) Time-averaged amplitude ($\tilde{p}_{\mathrm{rms}}$) envelopes are drawn symmetrically with respect to zero mean pressure; time-dependent ($\tilde{p}(t) \equiv \tilde{p}_{\mathrm{rms}}(t)$) amplitudes are indicated by the shaded areas. For all cases shown in figures 4(*a–c*), the leading tap on the top face is set arbitrarily at 0° phase.

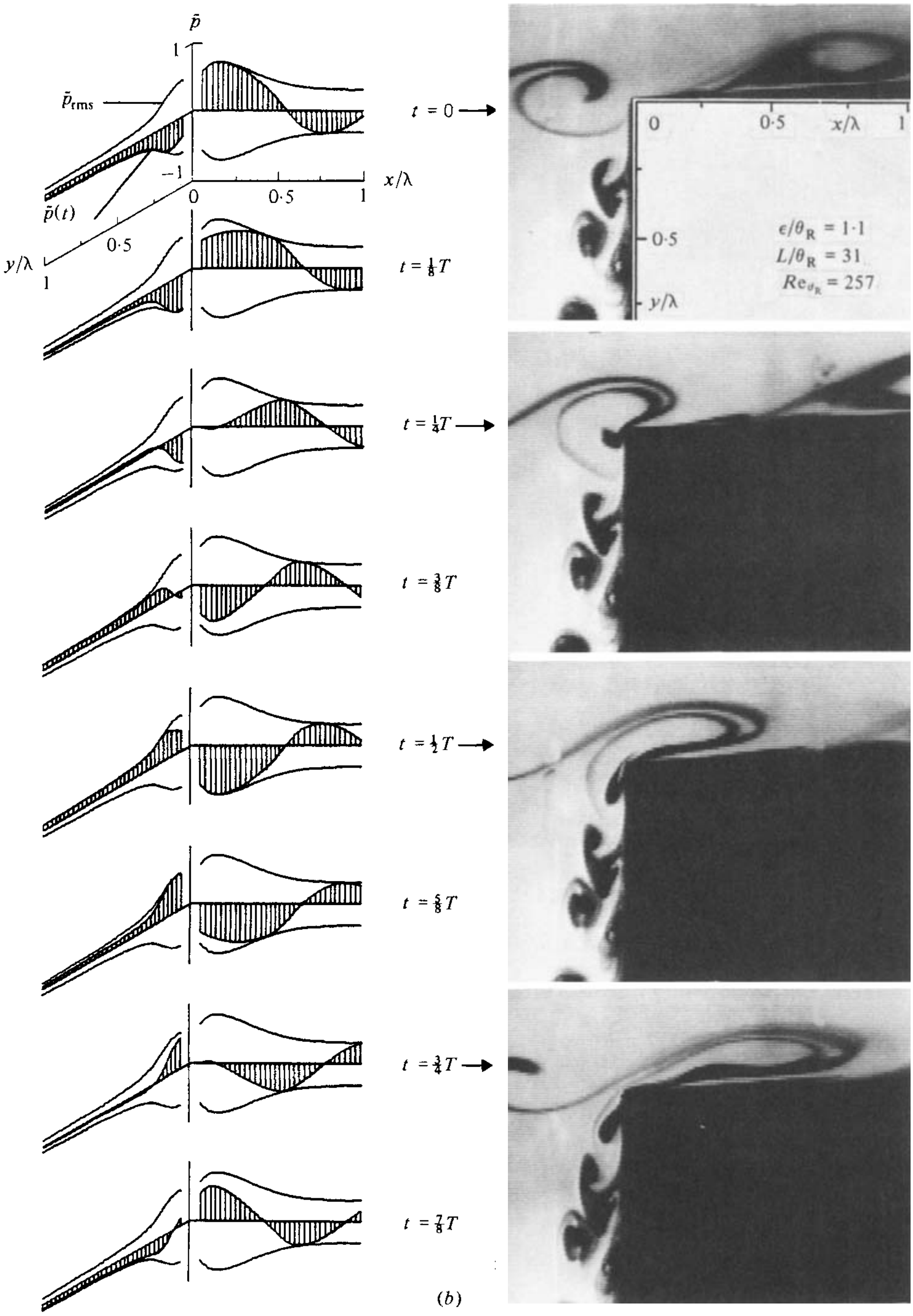

FIGURE 4. For caption see facing page.

Flow visualization by dye injection was recorded using the video system to allow correlation of the instantaneous pressure fields with the visualized incident vortex. Using the dual-camera split-screen capability of the video system, the original video recordings displayed simultaneously the visualized flow and pressure traces from the active pressure taps. Selected visualization photos are included in figure 4, covering

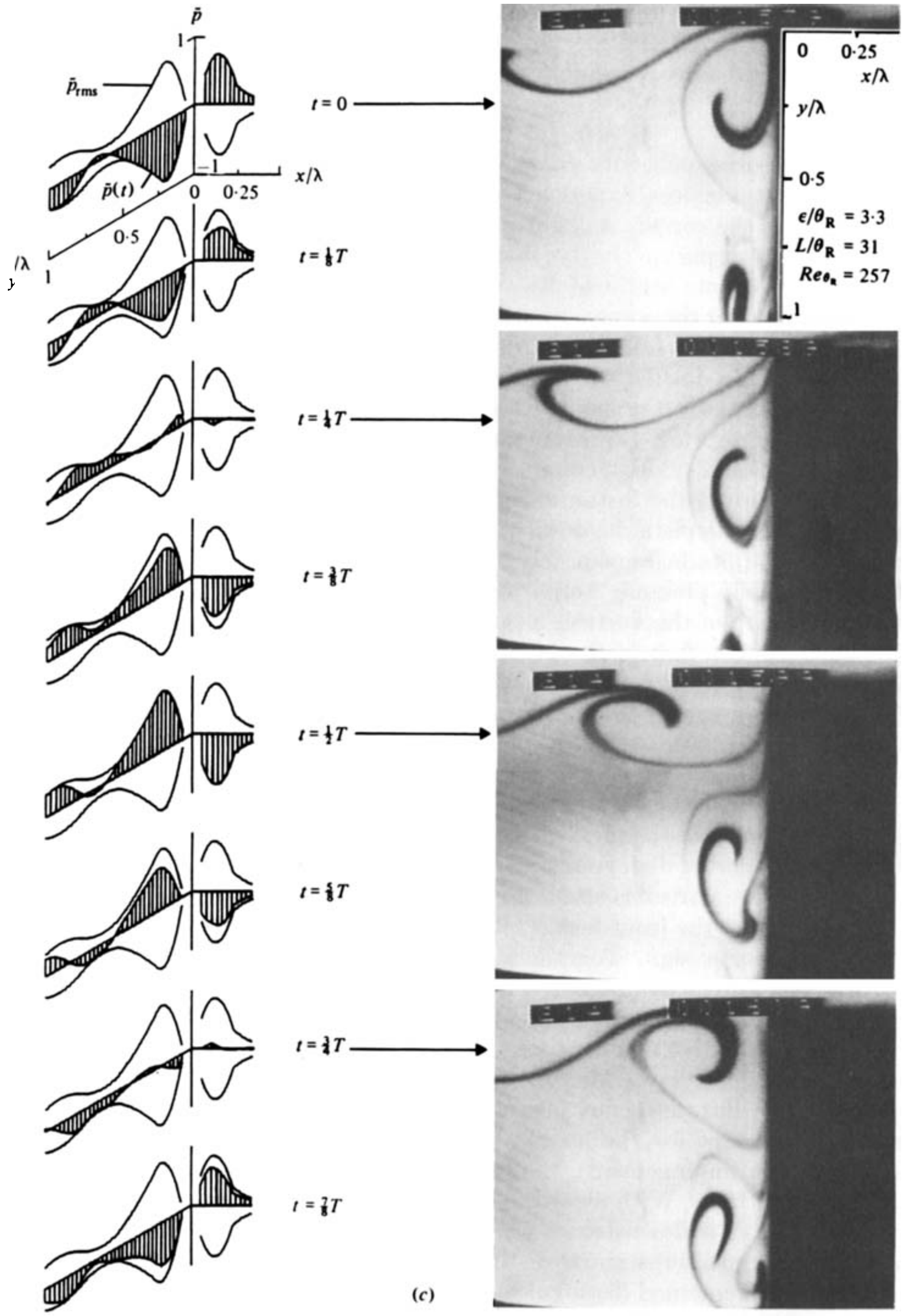

FIGURE 4. Instantaneous pressure distributions on top (x) and front (y) faces of the corner over 1 cycle of oscillation, along with simultaneous dye visualization at $L/\theta_R = 31$: (a) $\epsilon/\theta_R = -1{\cdot}1$; ($b$) 1·1; ($c$) 3·3.

the cyclic event at intervals of $\frac{1}{4}$ cycle. All these photos have the same scale and cover a total distance of $\sim \lambda$ along the top and front faces of the corner, corresponding to the domain of pressure measurement.

4.1. *Vortex above corner*

For the negative corner offset of $\epsilon/\theta_R = -1{\cdot}1$, visualization photos of figure 4(*a*) show that the incident vortices experience very minor distortion as they are swept downstream past the corner. A slight distortion of the incident vortex in the form of a kink in the lower part of the dye marker is evident as the vortex passes the edge. Careful frame-by-frame study of the video recordings suggest that the vortices actually climb up over the corner, whereby the centre of a typical vortex is gradually displaced approximately $1{\cdot}5\theta_R$ upwards; this occurs over a streamwise distance of $\sim 0{\cdot}3\lambda$ upstream and downstream of the edge of the corner, and is due to the image vortex within the corner (Conlisk & Rockwell 1981). Such climbing is evident in the $t = 0$ photo of figure 4(*a*). Downstream of the edge, elongation of vortices in the streamwise direction is evident, enhanced by viscous effects at the wall. In figure 4(*a*) the wavelike nature of the instantaneous pressure distributions along the top face of the corner clearly depicts the downstream convection of vortices. There is a rapid rise of pressure amplitude immediately downstream of the edge. Subsequent decrease and levelling off of pressure amplitude further downstream is associated with increased distortion of the vortices as they interact with the viscous wall layer. In contrast with the top face of the corner, there is an exponential drop of pressure amplitude along the front face; moreover, pressure fluctuations away from the edge ($y/\lambda \gtrsim 0{\cdot}5$) are seen to respond instantaneously at all locations.

4.2. *Vortex at corner*

Figure 4(*b*) illustrates the case of a small positive offset $\epsilon/\theta_R = 1{\cdot}1$. Visualization shows that the centre of the incident vortex is at essentially the same height as the edge. Substantial vortex distortion and apparent severing at the edge is evident. The lower portion of the vortex is swept downwards along the front face of the corner; flow separation from the front face is quickly induced, producing a concentration of vorticity of opposite sign. Together, these concentrations of vorticity form a counter-rotating vortex pair. There is little subsequent development of each vortex pair; moreover, these counter-rotating vortex pairs appear to 'stack up' owing to their very low convective speed, consistent with the small phase variation along the front face. Finally, vortex breakdown into turbulence was observed deep inside the cavity. From the instantaneous pressure distributions shown in figure 4(*b*), it is apparent that, except for the leading region of the front face (which is directly exposed to vortex impingement), the front face experiences nearly constant phase of pressure fluctuations. With regard to the top face of the corner, the portion of the clipped vortex that is downstream gives rise to a wavelike variation of pressure. Although it undergoes substantial distortion, visualization showed that this entity of rotational fluid remained distinguishable within several disturbance wavelengths downstream of the corner. Comparison of the $\tilde{p}(t)$ versus x/λ variations of figure 4(*b*) with those of figure 4(*a*) reveals that the form of the amplitude distributions as well as the phasing of the top-face pressure fields are similar, the absolute amplitude being smaller for the case of figure 4(*b*) because only a portion of the incident concentration of vorticity is swept downstream (i.e. figure 4*b*).

4.3. *Vortex below corner*

At the largest positive offset $\epsilon/\theta_{\mathrm{R}} = 3{\cdot}3$, the vortex–corner interaction takes place primarily along the front face of the corner, as shown in figure 4 (*c*). The approaching vortex is severely distorted against the front face of the corner, then is swept downward into the cavity along the front surface. This distortion of the vortex gives rise to the first large peak of the pressure amplitude, having an extent corresponding approximately to the apparent diameter of the incident vortex. Subsequent downward motion of the distorted vortex results in an eruption of a counter-rotating secondary vortex from the wall region. In the corresponding pressure composites, it is evident that the secondary peak in the pressure distribution (at $y/\lambda \gtrsim 0{\cdot}75$) along the front face is associated with this secondary vortex activity. Along the top face of the corner, the pressure amplitude rises and drops off sharply. Since the signal-to-noise ratio of the pressure fluctuations was relatively small (except very near the edge), amplitude and phase distributions in the region $x \gtrsim 0{\cdot}35\lambda$ were not considered to be sufficiently accurate to be shown here. However, near the edge, the pressure fluctuation is well-defined. In fact, examination of the instantaneous pressure fields of figure 4 (*c*) shows that the maximum pressure amplitudes on the top and front faces of the corner are π out of phase throughout the oscillation cycle, suggesting a well-defined dipole-like behaviour.

In order to understand better the mechanism of flow around the edge, dye was introduced into the cavity from an existing pressure tap (0·16 cm from the edge) on the front face. Figure 5 shows the close-up visualization, along with the corresponding overall vortex-impingement patterns. Four photos were taken at equal time intervals to cover approximately one-half an oscillation cycle, along with the corresponding overall vortex-impingement patterns. The dye from the front pressure tap is seen to move upwards towards the edge, then separate to form a small vortex travelling downstream over the top face of the corner. The concentrated vorticity associated with this vortex has the same sense and a scale about one-tenth that of the large-scale incident vortices. Associated with this leading-edge separation process is a relatively large pressure peak on the top face as shown in figure 4(*c*).

4.4. *Effects of larger streamwise lengthscale L*

Since the maturity, or degree of vorticity concentration, and therefore circulation Γ, of the incident vortex is a function of the impingement lengthscale L, its effective offset relative to the impingement corner ($\epsilon/\theta_{\mathrm{R}}$) can be expected to change with length L owing to its image within the corner (Ziada & Rockwell 1982; Conlisk & Rockwell 1981; Rogler 1974). Shown in figure 6 is a visualized sequence covering nearly two cyclic events of vortex impingement at a geometrical offset of $\epsilon/\theta_{\mathrm{R}} = 1{\cdot}1$ for a longer cavity length ($L = 40\theta_{\mathrm{R}}$). As shown, the impingement pattern is characterized by more mature roll-up of the incident vortex. The first incident vortex (see $t = 0$ photo) is clipped slightly below its centre to form a strong counter-rotating vortex pair along the front face; however, the second incident vortex (see $t = T$ photo) approaches the corner at a slightly higher position, and no such counter-rotating vortex pair evolves. In general, it was found that, at such longer cavity lengths, the vortex interactions at impingement exhibited the sort of variation shown in figure 6. In such cases, the time-averaged measuring techniques employed in this study do not accurately represent the corresponding flow events, characterized by several frequency components (Knisely & Rockwell 1982); consequently, instantaneous pressure fields were not pursued for longer cavity lengthscales than those employed for studies described in figures 3–5.

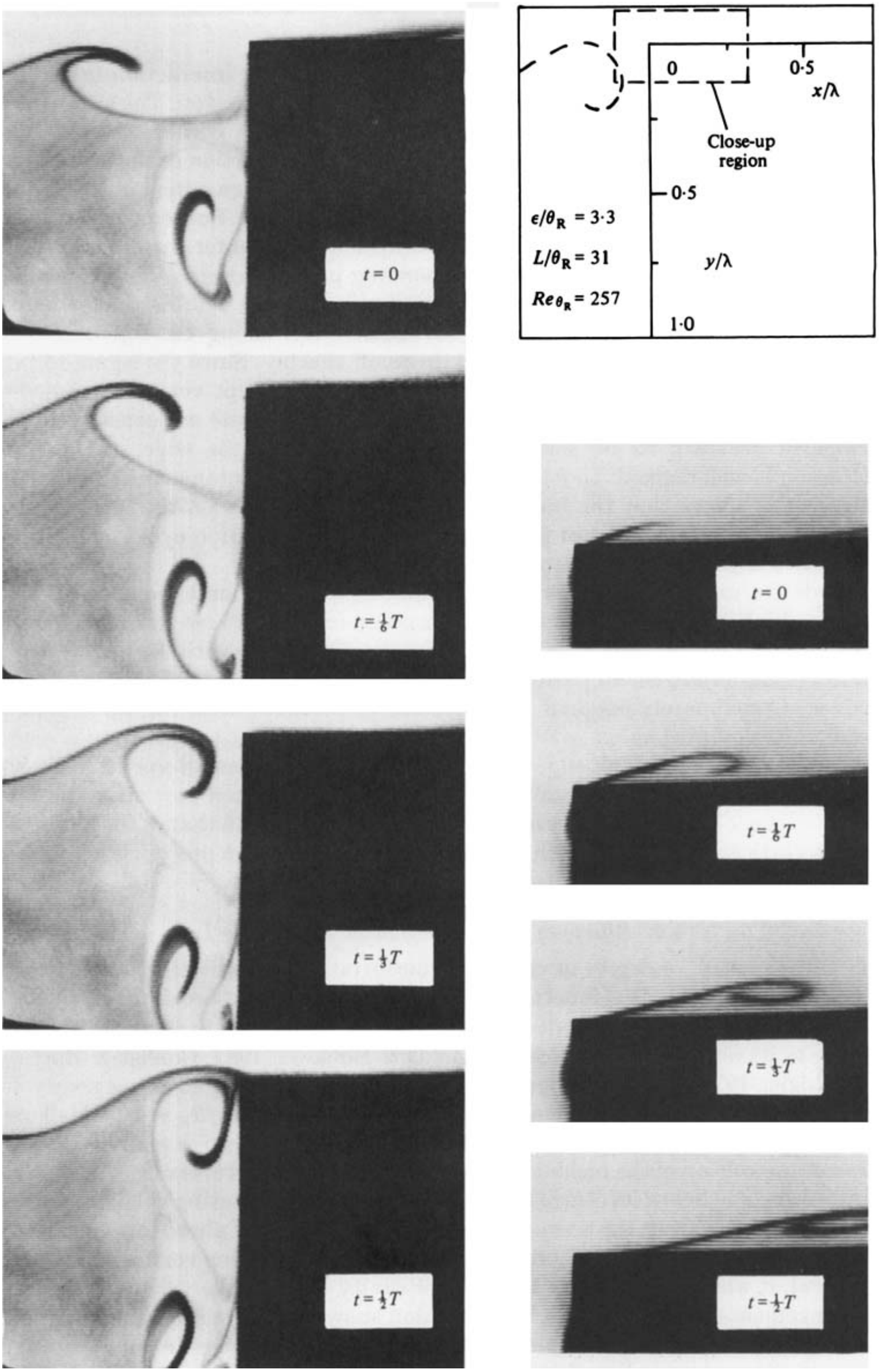

FIGURE 5. Visualization of impingment of incident vortex and close-up view of vortex shedding from leading edge of corner at $\epsilon/\theta_R = 3{\cdot}3$ and $L/\theta_R = 31$.

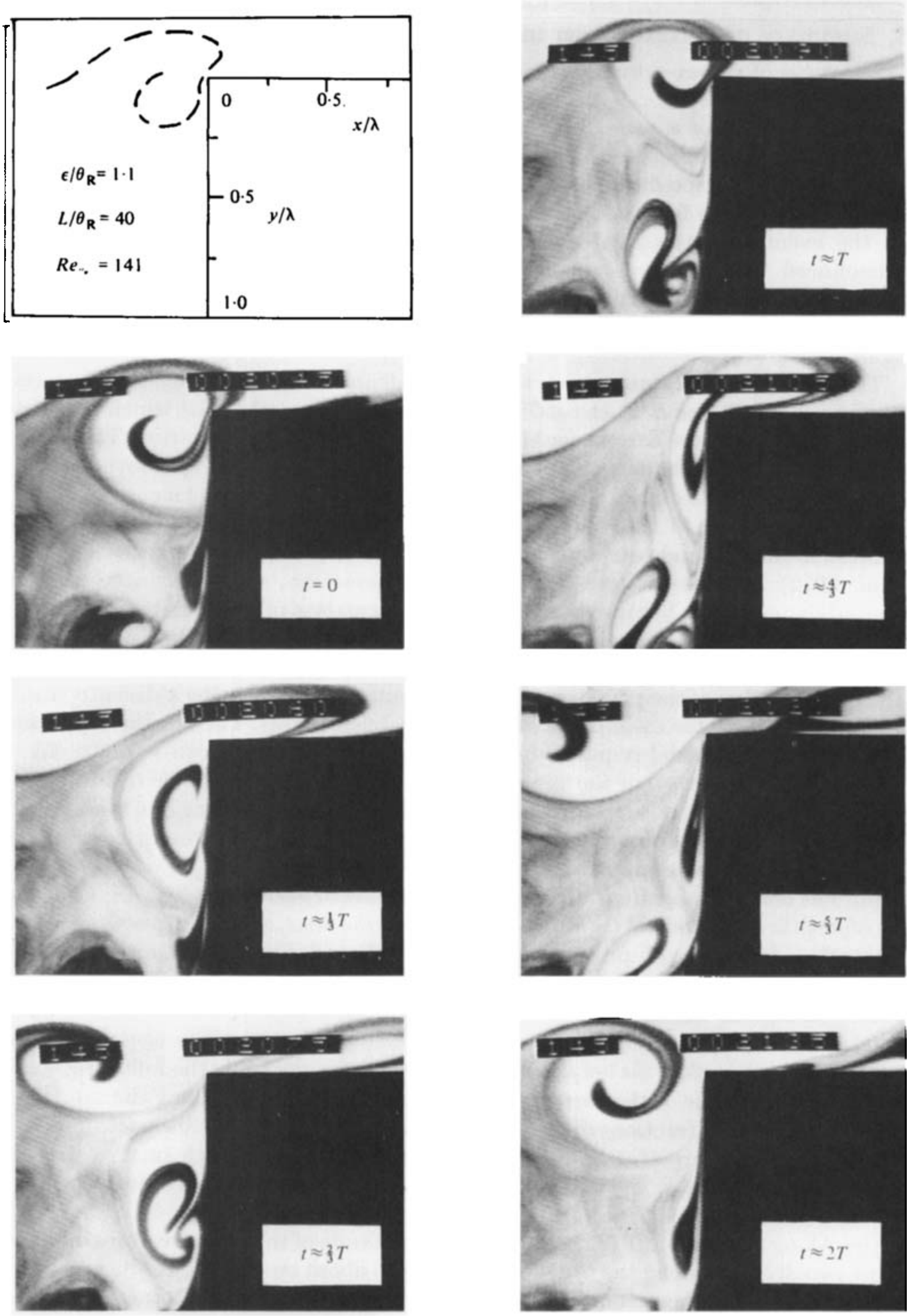

FIGURE 6. Vortex–corner interaction and eruption of vortex from front face of corner at $\epsilon/\theta_R = 1{\cdot}1$ and $L/\theta_R = 40$.

5. Summary of vortex–corner interaction mechanisms

The range of vortex–corner interactions described and shown in figures 4–6 suggest the following concepts.

(*a*) *As the core of a vortex impinges upon and is swept past a corner, it induces pronounced negative pressure, both on front and top faces near the edge of the corner.* This is dramatically depicted for the front face in figures 4(*a*) ($t = \frac{1}{4}T$), (*b*) ($t = \frac{1}{4}T$) and (*c*) ($t = 0$). For the top face, it is shown in figures 4(*a*) ($t = \frac{1}{2}T, \frac{7}{8}T$) and (*b*) ($t = \frac{1}{2}T, \frac{3}{4}T$). In the event that the incident vortex impinges below the corner, there is also pronounced negative pressure on the front face, shown in figure 4(*c*) ($t = 0$); moreover, the eventual eruption of the boundary layer produces a counter-rotating vortex that induces a negative pressure at the y/λ location of its centre, depicted in figure 4(*c*) ($t = \frac{7}{8}T$).

These observations agree with intuitive as well as conceptual models of convecting vortices (Lau, Fisher & Fuchs 1972; Lush 1973; Fuchs 1973), for which no direct visualization–pressure correlations have been available for confirmation. Theoretical simulations include the phasing of pressure fluctuations induced by convection of a single, discrete vortex in a free jet (Lush 1973; Fuchs 1973) and past a corner (Conlisk & Rockwell 1981). In the case of the free jet, a negative pressure perturbation is induced in the core and entrainment region as the centre of the vortex passes by (Lau *et al.* 1972); for the discrete vortex–corner interaction, such phasing cannot be accurately predicted, because the nature and deformation of the distributed vorticity of the incident vortex is dominant (Conlisk & Rockwell 1981). However, for the vortex travelling intact along the top face of the corner, the minor deformation of the vortex allows simulation of the phasing of induced negative pressure using a discrete vortex and its image, as, for example, carried out by Lush (1973). Though the amplitude predicted by his model requires modification to account for mean-velocity effects (Fuchs 1973) the phase of the pressure relative to location of centre of the vortex is properly predicted, also in agreement with the intuitive model of Lau *et al.* (1972), and the experimental observations herein: i.e. the centre of the vortex corresponds to maximum negative pressure (see e.g. figure 4*a*).

(*b*) *The order of magnitude of the maximum pressure fluctuation* $\tilde{p}_{\max}$ *induced near the edge of the corner on both the top and front faces is the same, and is* $\tilde{p}_{\max} = O(\rho\tilde{u}_{\max}U)$, where $\tilde{u}_{\max}$ is the maximum r.m.s. amplitude of the velocity fluctuation in the shear layer just upstream of impingement and U is free-stream velocity. It can take on values as high as $2{\cdot}8\rho\tilde{u}_{\max}U$.

(*c*) *In cases where a significant fraction of the incident vorticity concentration is swept downstream along the top face of the corner* (e.g. figures 4*a*, *b*) the following occur.

(i) The amplitude of the corresponding pressure fluctuations along the top face is smaller for smaller fractions of the concentrated vorticity swept downstream (figure 4(*b*) relative to figure 4(*a*)). This trend is associated not only with smaller strength (circulation), but also increased distortion of the vorticity concentration swept downstream (compare figure 4(*b*) with figure 4(*a*)).

(ii) Along the front face of the corner, the amplitude of the pressure drops off much more rapidly than along the top face, decaying to about one-quarter of its maximum value within a distance of one-half wavelength from the edge of the corner (see figures 4*a*, *b*). Away from the edge of the corner, pressure fluctuations tend to be in phase at all spatial locations along the front face.

(*d*) *In the event that nearly all of the incident vorticity is swept below the corner* (see figure 4*c*), the following are evident.

(i) Maximum pressure amplitude occurs at the location of the centre of the vortex (see figure 4(*c*), $t = 0$); moreover; eventual eruption of the boundary layer from the front face results in formation of a counter-rotating vortex pair and a secondary maximum of fluctuating pressure (see figure 4(*c*), $t = \frac{7}{8}T$).

(ii) This counter-rotating vortex pair travels downwards along the front face ($y/\lambda \gtrsim 0{\cdot}7$) with a phase speed $c_{\mathrm{v}}/U = 0{\cdot}25$.

(iii) Very near the edge of the top face of the corner, large-amplitude pressure fluctuations are induced, being associated with flow separation from the edge; downstream of this region, the pressure amplitudes are extremely small (see figure 4*c*).

6. Unsteady forces and moments on the corner

Unsteady forces on the corner can be examined by integrating instantaneous pressure distributions of figures 4(*a–c*) on each surface of the corner. To illustrate the effects of the extent of the integration domain on the resultant force, integrations were carried out over the leading 25 %, 50 %, 75 % and a full 100 % of the pressure measurement domain, corresponding respectively to $\frac{1}{4}$, $\frac{1}{2}$, $\frac{3}{4}$ and 1 wavelengths λ of the incident disturbance. Resultant forces, normalized with respect to the maximum value of all three corner offsets ($\epsilon/\theta_{\mathrm{R}} = 1{\cdot}1$, $1{\cdot}1$ and $3{\cdot}3$) are given in figures 7(*a–c*). As a larger share of the incident vortex is severed and swept down into the cavity (see figures 4*a–c*), there is increased tendency for the instantaneous forces on the top and front surfaces of the corner to be π out of phase. In fact, for the case where nearly all of the incident vortex is swept downwards ($\epsilon/\theta_{\mathrm{R}} = 3{\cdot}3$), the maximum deviation from this π phase condition is only $0{\cdot}12\pi$ (see figure 4*c*), regardless of the size of the domain over which the pressure is integrated. The physical reason for this remarkably consistent π phase difference can be seen by examining the instantaneous pressure distributions of figure 4(*c*). On the top and front faces, the dominant fluctuation amplitudes occur very near the edge, and are π out of phase; moreover, the amplitude of the secondary peak on the front face (at $y/\lambda = 0{\cdot}8$) is relatively small and tends to be in phase with the dominant peak on that face (at $z/\lambda = 0{\cdot}25$). As for the cases where the incident vortex is severed at ($\epsilon/\theta_{\mathrm{R}} = 1{\cdot}1$), or passes over ($\epsilon/\theta_{\mathrm{R}} = -1{\cdot}1$) the edge, there is deviation from this π phase difference, though the general tendency for the forces on the front and top faces to be out of phase is evident.

Integrated elemental moments acting on the corner, associated with the instantaneous pressure distributions on the corner, are determined by taking elemental moments about the point of intersection (inside the corner) of two perpendicular lines drawn through $x/\lambda = 1$ and $\theta/\lambda = 1$ (see figure 5 for terminology). Results are presented in a similar manner as for the force fluctuations, using four different-sized domains. Fluctuating moments for corner offsets $\epsilon/\theta_{\mathrm{R}} = -1{\cdot}1$, $1{\cdot}1$ and $3{\cdot}3$ are shown in figures 8(*a–c*). In general, the fluctuating moments are found to have very similar magnitudes and are not strongly influenced by the size of domain for all three corner offsets. However, there is significant phase difference of these fluctuating moments; as the offset increases, the phase of the moments advances.

7. Conclusions

For the case of unstable flow past a cavity examined herein, small transverse offsets of the downstream corner of the cavity (of the order of local momentum thickness) have an insignificant effect on the frequency, phase speed and the wavelength of the

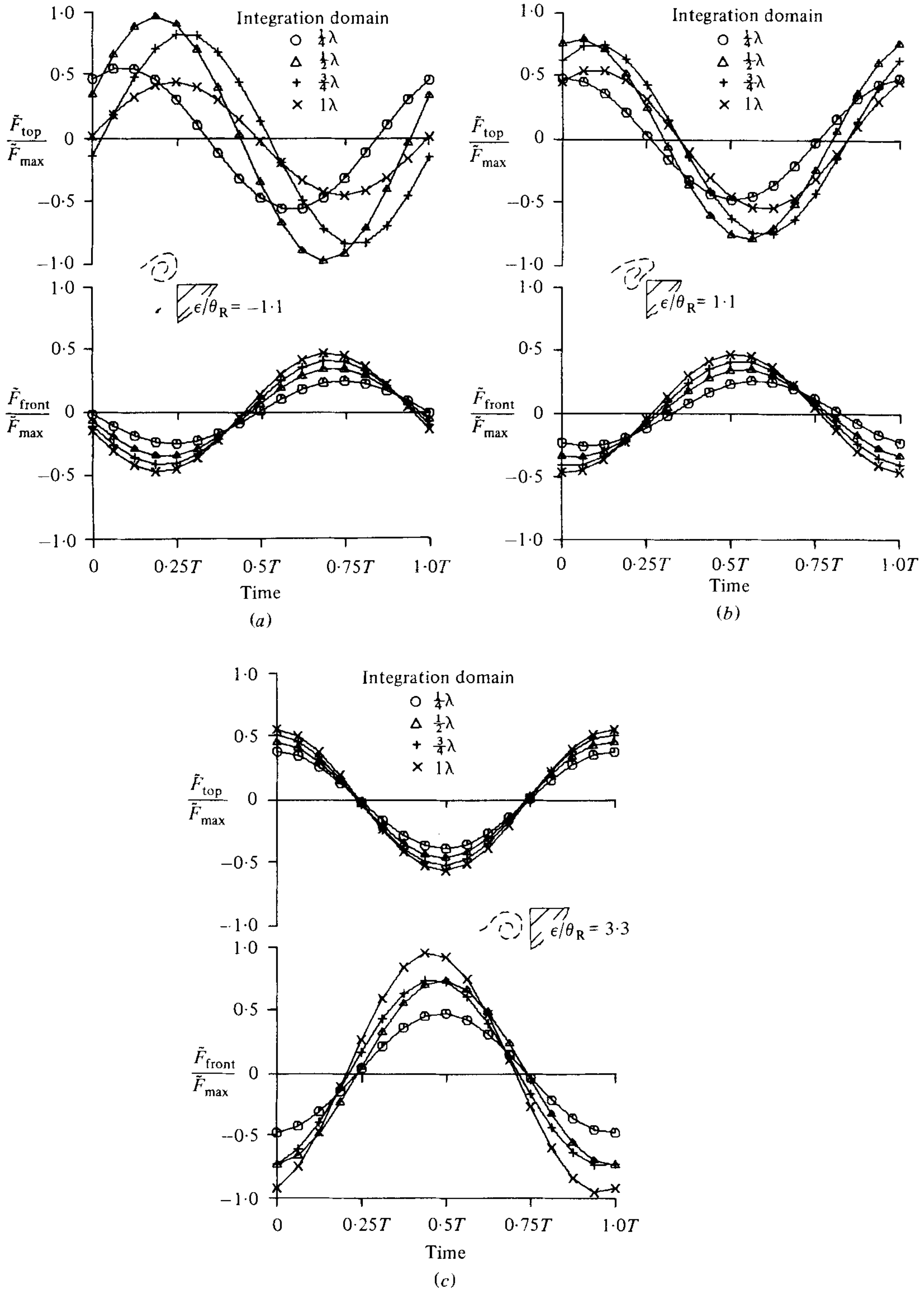

FIGURE 7. Periodic forces $\tilde{F}$ on top and front faces of the corner as a function of size of integration domain; $L/\theta_R = 31$: (a) $\epsilon/\theta_R = -1\cdot1$; (b) $1\cdot1$; (c) $3\cdot3$.

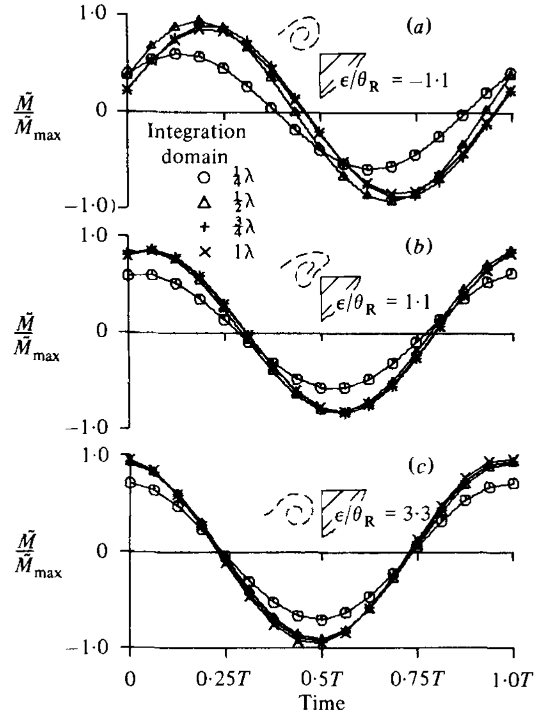

FIGURE 8. Fluctuating moment $\tilde{M}$ about the intersection point ($x/\lambda = 1$, $y/\lambda = 1$) as a function of size of integration domain for $L/\theta_R = 31$: (a) $\epsilon/\theta_R = -1\cdot1$; (b) $1\cdot1$; (c) $3\cdot3$. $\tilde{M}_{max}$ has the same value for all ϵ/θ_R.

vortices. This insensitivity provided consistent conditions of the approach vortices for all values of the corner offset, allowing a direct comparison of the vortex–corner interaction mechanism for similar approach flow conditions.

Depending upon the offset of the downstream corner of the cavity, and consequently the mechanism of incident vortex–corner interaction, one of two general types of vortex shedding from the downstream corner of the cavity could be observed. For the first type, vorticity was shed from the edge of the corner owing to perturbation of the corner flow by the incident vortex, had the same sense as the incident vortex, and was convected downstream along the upper surface of the corner. Regarding the second type of shed vortex, it is associated with eruption of the viscous wall layer of the front face of the corner, due to the severe fluctuating pressure gradient produced by the incident vortex. Both of these classes of shed vortices have important consequences for the fluctuating pressure distribution at the corner.

In cases where the incident vortex is only mildly distorted, the occurrence of minimum negative pressure along the surface of the corner is in accordance with potential theory: it coincides approximately with the centre of the concentration of vorticity. In all cases, including those where severe distortion of the incident vortex occurs, the order of magnitude of the maximum pressure fluctuation is $\rho\tilde{u}_{max}U$, where $\tilde{u}_{max}$ corresponds to the maximum velocity fluctuation amplitude just upstream of the corner, and U represents the free-stream velocity.

Consideration of the instantaneous forces acting on the top and of the front faces of the corner, obtained by integrating the instantaneous pressure variations, shows that as a larger share of the incident vortex is severed and swept down into the cavity, the instantaneous forces on the top and front surfaces of the corner tend increasingly to be π out of phase. With regard to the fluctuating moments acting on the corner, their magnitude is found to be relatively insensitive to the corner offset; but there is a significant phase difference between these fluctuating moments, the phase of the moments tending to advance with increasing offset.

This investigation was supported by the National Science Foundation of Washington, D.C., and the Volkswagen Foundation of Hannover, West Germany. All experiments were carried out at Lehigh University; the authors appreciate the help of Fred Wehden and Dick Towne in manufacturing the rotating pressure valve.

This paper was written while D.R. was an Overseas Fellow of Churchill College at Cambridge University.

REFERENCES

CONLISK, T. & ROCKWELL, D. 1981 Modelling of vortex–corner interaction using point vortices. *Phys. Fluids* **24**, 2133–2142.

FUCHS, H. V. 1973 Comments on 'The pressure and velocity fields of convected vortices'. *J. Sound Vib.* **30**, 249–251.

KNISELY, C. & ROCKWELL, D. 1982 Self-sustained low-frequency components in an impinging shear layer. *J. Fluid Mech.* **116**, 157–186.

LAU, J. C., FISHER, M. J. & FUCHS, H. V. 1972 The intrinsic structure of turbulent jets. *J. Sound Vib.* **22**, 379–406.

LUSH, P. A. 1973 The pressure and velocity fields of convected vortices. *J. Sound Vib.* **27**, 266–270.

MICHALKE, A., 1965 On spatially growing disturbances in an inviscid shear layer. *J. Fluid Mech.* **23**, 521–544.

ROCKWELL, D. 1982 Oscillations of impinging shear layers. Invited lecture at A.I.A.A. 20th Aerospace Sciences Meeting, 11–13 January. Available as *A.I.A.A. Preprint* 82-0047. *A.I.A.A. J.* (to be published 1983).

ROCKWELL, D. & KNISELY, C. 1979 The organized nature of flow impingement upon a corner. *J. Fluid Mech.* **93**, 413–432.

ROGLER, H. 1974 A mechanism of vorticity segregation. *Bull. Am. Phys. Soc., Ser. II*, **19**, 1165.

ROGLER, H. 1978 The interaction between vortex-array representations of free-stream turbulence and semi-infinite flat plates. *J. Fluid Mech.* **87**, 583–606.

ROSHKO, A. 1976 Structure of turbulent shear flows: a new look. *A.I.A.A. J.* **14**, 1349–1357.

TANG, Y.-P. 1981 Correlation of pressure fluctuations at an impingement corner due to vortex–corner interaction. M.S. thesis, Department of Mechanical Engineering and Mechanics, Lehigh University.

ZIADA, S. & ROCKWELL, D. 1982 Vortex–leading-edge interaction. *J. Fluid Mech.* **118**, 79–107.